J. Phys. B: At. Mol. Opt. Phys. **44** (2011) 184018 (7pp) doi:10.1088/0953-4075/44/18/184018

Quantum interference in interacting three-level Rydberg gases: coherent population trapping and electromagnetically induced transparency

S Sevinçli[1], C Ates[1,2], T Pohl[1], H Schempp[3], C S Hofmann[3], G Günter[3], T Amthor[3], M Weidemüller[3], J D Pritchard[4], D Maxwell[4], A Gauguet[4], K J Weatherill[4], M P A Jones[4] and C S Adams[4]

[1] Max Planck Institute for the Physics of Complex Systems, Nöthnitzer Strasse 38, 01187 Dresden, Germany
[2] Midlands Ultracold Atom Research Centre, School of Physics and Astronomy, The University of Nottingham, Nottingham, NG7 2RD, UK
[3] Philosophenweg 12, 69120 Heidelberg, Physikalisches Institut der Universität Heidelberg, Germany
[4] Department of Physics, Durham University, Rochester Building, South Road, Durham DH1 3LE, UK

E-mail: tpohl@pks.mpg.de, weidemueller@physi.uni-heidelberg.de and c.s.adams@durham.ac.uk

Received 10 February 2011, in final form 13 June 2011
Published 14 September 2011
Online at stacks.iop.org/JPhysB/44/184018

Abstract
In this paper, we consider the effects of strong dipole–dipole interactions on three-level interference phenomena such as coherent population trapping and electromagnetically induced transparency. Experiments are performed on laser cooled rubidium atoms and the results compared to a many-body theory based on either a reduced many-body density matrix expansion or Monte Carlo simulations of many-body rate equations. We show that these approaches permit quantitative predictions of the experimentally observed excitation and transmission spectra. Based on the calculations, we moreover predict a universal scaling of the nonlinear response of cold Rydberg gases.

(Some figures in this article are in colour only in the electronic version)

1. Introduction

Quantum interference in driven multi-level systems gives rise to a range of remarkable phenomena, being explored in various different physical settings, ranging from quantum dots and optical fibres to optomechanical systems and cold atomic gases [1–9]. In the simple case of a three-level atom coherently coupled to two laser fields, interference between the two excitation pathways has profound consequences for the atomic state evolution as well as for the propagation of the applied optical fields. This leads to coherent population trapping (CPT) [10] into a quantum superposition of the atomic states which is independent of the intermediate level. Hence, the atom becomes transparent to the laser fields, being referred to as electromagnetically induced transparency (EIT) [5, 11]. For non-interacting atomic gases, these related effects have been studied intensively, as they provide a promising basis for storing [12, 13] and manipulating [14] quantum information as well as precision spectroscopy [15].

More recently, it has been recognized that the combination of EIT and highly excited Rydberg states [16] opens up new perspectives for such applications. Theoretically, strongly interacting Rydberg atoms driven in an EIT configuration were shown to enable the generation of non-classical light [17, 18] and many-atom entanglement [19, 20] and to permit implementation of photonic phase gates [21] and quantum simulators for exotic many-body systems [22]. Experiments have studied the effect of Rydberg–Rydberg atom interactions on EIT and CPT [23–27]. The experimental demonstration of a giant Kerr effect [24] based on the exaggerated polarizability

of Rydberg atoms and huge dissipative optical nonlinearities [27] due to strong Rydberg–Rydberg atom interactions already demonstrates the great potential of Rydberg-EIT media for applications in quantum optics.

To illustrate the physical mechanism of CPT and EIT, consider first a single three-level atom composed of a ground state $|1\rangle$, a rapidly decaying intermediate state $|2\rangle$ and a highly excited Rydberg state $|3\rangle$. Within a ladder configuration, the states $|1\rangle$ and $|3\rangle$ are coherently coupled to the common intermediate state $|2\rangle$ and the decay of the Rydberg state $|3\rangle$ is negligible slow (cf figure 1). Consequently, on two-photon resonance, the system evolves into the dark state

$$|d\rangle = \frac{1}{\sqrt{\Omega_1^2 + \Omega_2^2}}(\Omega_2 |1\rangle - \Omega_1 |3\rangle), \tag{1}$$

which is not affected by the excitation lasers and is immune to radiative decay of the intermediate state. Consequently, this leads to a narrow, subnatural Rydberg excitation line (CPT), as well as dissipationless propagation of the optical fields (EIT). This simple picture, however, gets modified already for two atoms with Rydberg state interactions. Most importantly, the simultaneous Rydberg excitation of both atoms gets blocked once the interaction energy exceeds the corresponding excitation linewidth (see figure 1(b)). As a consequence, this interaction- or dipole-blockade [28] modifies the two-atom dark state [19], and thus affects the Rydberg-CPT line as well as the light transmission on the EIT resonance.

From the dark state (1) we can distinguish two different cases. If $\Omega_1 \gg \Omega_2$ (case A in figure 1) the majority of atoms are transferred into Rydberg states, suggesting a dramatic effect of Rydberg–Rydberg interaction on their excitation dynamics. In the opposite case (case B in figure 1) most of the population resides in the ground state, with interaction effects arising from the small admixture ($\sim\Omega_1^2/\Omega_2^2$) of Rydberg states. In this work, we present a combined experimental and theoretical investigation of the effect of Rydberg state interactions on CPT and EIT that covers both of these regimes. In the experiments we work with Rydberg S states since due to their repulsive interaction, as indicated in figure 1(b), these atoms are relatively stable against ionizing collisions [29], and since they do not undergo significant state mixing [30, 31] due to dipole–dipole coupling to adjacent pair states. Section 3 presents Rydberg excitation spectra for case A, which reveal an unshifted CPT line despite a strong interaction-induced suppression of Rydberg excitation. Measurements of the optical transmission, presented in section 4 for the opposite case B, demonstrate the emergence of strongly nonlinear absorption due to Rydberg–Rydberg atom interactions but an otherwise unshifted transmission line. These findings are well reproduced by the theoretical calculations, outlined in section 2, which generally show very good agreement with the experimental data.

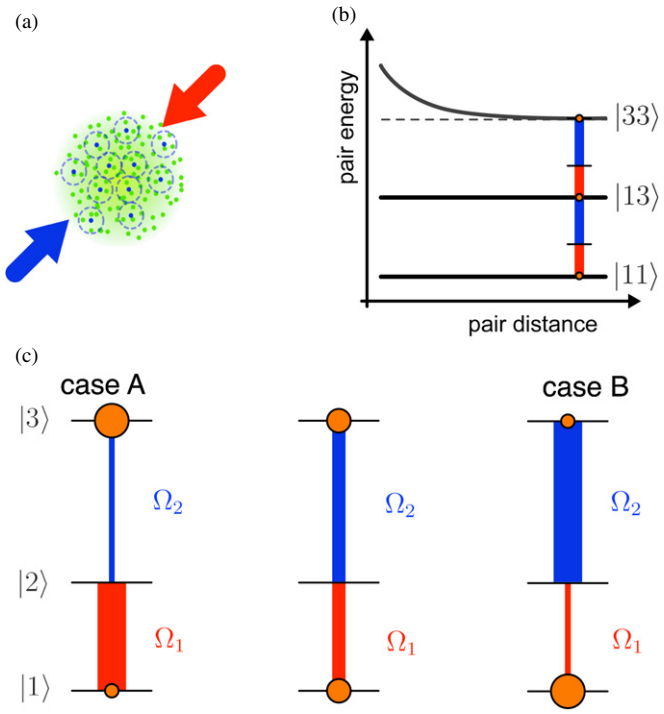

Figure 1. Due to van der Waals interaction the pair energy of two Rydberg atoms is bent at short interatomic separations (b), which leads to a suppression of excitation around an already excited Rydberg atom. (a) In a gas of atoms this gives rise to avoided volumes in which only one Rydberg atom can be excited, as indicated by the dashed circles. (c) Depending on the ratio of the two Rabi frequencies different characters of the dark state can be realized. In the extreme case of a very small upper Rabi frequency Ω_2 (case A) the dark state is largely composed of the Rydberg state whereas for a very small lower Rabi frequency Ω_1 (case B) the dark state is dominated by the ground state. The corresponding populations are indicated by the size of the spheres in (c).

2. Many-body theory

Extending the above single-body discussion, we now consider a Rydberg gas composed of N interacting three-level atoms at positions $\mathbf{r}_i$. Starting from the underlying Heisenberg equations the dynamics of the corresponding atomic transition and projection operators $\hat{\sigma}_{\alpha\beta}^{(i)} = |\alpha_i\rangle\langle\beta_i|$ $(\alpha, \beta = 1, 2, 3)$ follows

$$\frac{\mathrm{d}}{\mathrm{d}t}\hat{\sigma}_{11}^{(i)} = \mathrm{i}\frac{\Omega_1^{(i)}}{2}\left(\hat{\sigma}_{12}^{(i)} - \hat{\sigma}_{21}^{(i)}\right) + \gamma\hat{\sigma}_{22}^{(i)}, \tag{2a}$$

$$\frac{\mathrm{d}}{\mathrm{d}t}\hat{\sigma}_{22}^{(i)} = -\mathrm{i}\frac{\Omega_1^{(i)}}{2}\left(\hat{\sigma}_{12}^{(i)} - \hat{\sigma}_{21}^{(i)}\right) + \mathrm{i}\frac{\Omega_2^{(i)}}{2}\left(\hat{\sigma}_{23}^{(i)} - \hat{\sigma}_{32}^{(i)}\right) - \gamma\hat{\sigma}_{22}^{(i)}, \tag{2b}$$

$$\frac{\mathrm{d}}{\mathrm{d}t}\hat{\sigma}_{33}^{(i)} = -\mathrm{i}\frac{\Omega_2^{(i)}}{2}\left(\hat{\sigma}_{23}^{(i)} - \hat{\sigma}_{32}^{(i)}\right), \tag{2c}$$

$$\frac{\mathrm{d}}{\mathrm{d}t}\hat{\sigma}_{12}^{(i)} = -\mathrm{i}\frac{\Omega_1^{(i)}}{2}\left(2\hat{\sigma}_{22}^{(i)} + \hat{\sigma}_{33}^{(i)} - 1\right) + \mathrm{i}\frac{\Omega_2^{(i)}}{2}\hat{\sigma}_{13}^{(i)} + \mathrm{i}\Delta_1\hat{\sigma}_{12}^{(i)} - \frac{\gamma + \gamma_{12}}{2}\hat{\sigma}_{12}^{(i)}, \tag{2d}$$

$$\frac{\mathrm{d}}{\mathrm{d}t}\hat{\sigma}_{13}^{(i)} = -\mathrm{i}\frac{\Omega_1^{(i)}}{2}\hat{\sigma}_{23}^{(i)} + \mathrm{i}\frac{\Omega_2^{(i)}}{2}\hat{\sigma}_{12}^{(i)} + \mathrm{i}(\Delta_1 + \Delta_2)\hat{\sigma}_{13}^{(i)} - \frac{\gamma_{12} + \gamma_{23}}{2}\hat{\sigma}_{13}^{(i)} - \mathrm{i}\sum_{j\neq i} V_{ij}\hat{\sigma}_{33}^{(j)}\hat{\sigma}_{13}^{(i)}, \tag{2e}$$

$$\frac{\mathrm{d}}{\mathrm{d}t}\hat{\sigma}_{23}^{(i)} = -\mathrm{i}\frac{\Omega_2^{(i)}}{2}\left(\hat{\sigma}_{33}^{(i)} - \hat{\sigma}_{22}^{(i)}\right) - \mathrm{i}\frac{\Omega_1^{(i)}}{2}\hat{\sigma}_{13}^{(i)} - \frac{\gamma+\gamma_{23}}{2}\hat{\sigma}_{23}^{(i)} + \mathrm{i}\Delta_2\hat{\sigma}_{23}^{(i)} - \mathrm{i}\sum_{j\neq i} V_{ij}\hat{\sigma}_{33}^{(j)}\hat{\sigma}_{23}^{(i)}, \qquad (2f)$$

where $\Delta_{1(2)}$ denote the detunings of the probe and coupling laser beams and the rate constants γ, γ_{12} and γ_{23} account for spontaneous decay of the intermediate level $|2\rangle$ as well as for finite bandwidths of the applied lasers. Their corresponding Rabi frequencies $\Omega_{1(2)}^{(i)}$ depend on the atomic positions $\mathbf{r}_i$ through the respective intensity profiles, i.e. $\Omega_{1(2)}^{(i)} = \Omega_{1(2)}(\mathbf{r}_i)$. We exclusively consider $|3\rangle = |n\mathrm{S}\rangle$ Rydberg states that interact via isotropic van der Waals potentials $V_{ij} = C_6/r_{ij}^6$.

In the non-interacting limit $V_{ij} = 0$, equations (2) reduce to the standard optical Bloch equations (OBEs) for independent three-level atoms, thus, leading to EIT and CPT as discussed above. The presence of Rydberg–Rydberg atom interactions, however, results in a strongly correlated many-body dynamics, whose exact description becomes prohibitively demanding already for moderate atom numbers N. In the following, we outline two complementary approximate treatments of (2) that are shown to account for our experimental findings.

2.1. Reduced density matrix expansion

Aiming at an approximate description of the excitation *dynamics* at moderate densities, we consider the time evolution of the reduced density matrix elements. Using the definitions $\rho_{\alpha\beta}^{(i)} = \langle\hat{\sigma}_{\alpha\beta}^{(i)}\rangle$, $\rho_{\alpha\beta,\alpha'\beta'}^{(i,j)} = \langle\hat{\sigma}_{\alpha\beta}^{(i)}\hat{\sigma}_{\alpha'\beta'}^{(j)}\rangle$, etc, their time evolution follows directly from (2). The resulting dynamical equations for the single-body elements $\rho_{\alpha\beta}^{(i)}$ involve two-body elements $\rho_{33,\alpha\beta}$, whose dynamics requires knowledge of three-body elements, and so on. Consequently, the resulting BBGKY hierarchy [32] has to be closed in an appropriate way. Here, we apply a second-order ladder approximation, such that the three-body interaction terms appearing in the two-body equation are expressed by [26]

$$\sum_{k\neq i,j} V_{jk}\rho_{33,\alpha\beta,\alpha'\beta'}^{(k,i,j)} = \sum_{k\neq i,j} V_{jk}\rho_{\alpha\beta}^{(i)}\rho_{33,\alpha'\beta'}^{(k,j)}\,. \qquad (3)$$

This procedure fully accounts for binary correlations and approximately includes many-body correlations at small mutual distances. The resulting $\mathcal{O}(N^2)$ coupled differential equations for the single- and two-body density matrices can be solved numerically and are used to describe our measurements of CPT dynamics presented in section 3. As one naturally expects from a density expansion its validity becomes questionable at high densities. In order to describe the high-density measurements of section 4, we, therefore, apply an alternative approach outlined below.

2.2. Monte Carlo rate equation approach

Being primarily interested in the many-body *steady states* of equations (2) one can resort to a rate equation treatment [33–35] whose validity is not restricted by the density of atoms. For clarity, we start from the non-interacting case, for which the N-particle density matrix factorizes into single-atom ones $\left(\rho_{\alpha\beta}^{(i)}\right)$. Upon adiabatic elimination of the coherences in the corresponding OBEs, the dynamics of the populations follows a set of rate equations

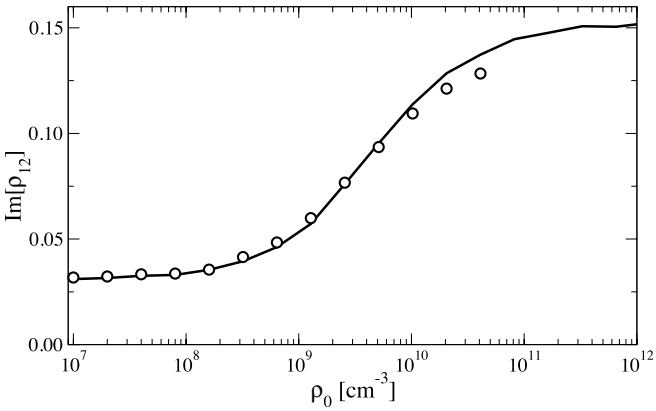

Figure 2. Density dependence of the imaginary part of the probe-transition coherence for a ^{87}Rb 55S Rydberg gas driven with $\Omega_1 = 1$ MHz and $\Omega_2 = 2$ MHz, with both laser beams chosen to be resonant and to have a linewidth of 100 kHz. Calculations based on the RDME (circles) and the MCRE approach (line) are shown for comparison.

$$\frac{\mathrm{d}}{\mathrm{d}t}\begin{pmatrix}\rho_{11}^{(i)}\\ \rho_{22}^{(i)}\\ \rho_{33}^{(i)}\end{pmatrix} = \begin{pmatrix}-a_{11} & a_{12} & a_{13}\\ a_{21} & -a_{22} & a_{23}\\ a_{31} & a_{32} & -a_{33}\end{pmatrix}\begin{pmatrix}\rho_{11}^{(i)}\\ \rho_{22}^{(i)}\\ \rho_{33}^{(i)}\end{pmatrix}, \qquad (4)$$

where the rate coefficients $a_{\alpha\beta}$ are obtained from the OBEs as a function of the laser parameters. This single-atom rate equation description is straightforwardly extended to interacting atoms by replacing the detuning Δ_1 by $\Delta_1^{(i)} = \Delta_1 + \sum_{i\neq j}' V_{ij}$, which accounts for the van der Waals shift induced by excited Rydberg atoms. The sum $\sum'$ runs over all atoms in state $|3\rangle$ such that $\Delta_1^{(i)}$, and, hence, the transition rates, depend on the actual many-body configuration of Rydberg atoms in the gas. As shown in [34], this replacement only neglects simultaneous multi-photon excitation of several Rydberg atoms, which typically can safely be neglected. Note that the resulting many-body rate equation still covers an exponentially large number of 3^N many-body states. Using a Monte Carlo propagation scheme [36], it can, however, be solved efficiently for very large numbers of atoms. This procedure yields the steady-state diagonal elements of the entire N-body density matrix. Using the average population $\rho_{22} = N^{-1}\sum_i \rho_{22}^{(i)}$ of the intermediate state together with equations (2*b*) and (2*c*) one can further determine $\Im[\rho_{12}] = \frac{\gamma}{\Omega_1}\rho_{22}$, which yields the nonlinear absorption of the probe beam, to be discussed in section 4. In figure 2, we compare the steady-state value of ρ_{12} as obtained from the two methods. Over a wide range of densities there is very good agreement between these entirely different approaches, providing strong support for the applied approximations. Expectedly, the density matrix expansion deviates at higher densities, but gives a good description up to surprisingly high densities of ($\rho \lesssim 10^{10}$ cm^{-3}). The Monte Carlo results, however, also yield the correct high-density limit [36], and should, hence, be applicable for arbitrary interaction strengths and densities.

3. CPT experiments

3.1. Experimental conditions

The experiments on CPT (see also [26]) are performed in a magneto-optical trap of ^{87}Rb atoms with peak densities of up to 6.6×10^9 cm^{-3}. Starting from the stretched state $5S_{1/2}(F = 2, m_F = 2)$ the atoms can be excited to Rydberg states in a two-photon excitation where the first photon at 780 nm couples the ground state to the intermediate state $5P_{3/2}(F = 3, m_F = 3)$. The second photon at around 480 nm can be tuned and thereby address different Rydberg states.

To enhance interaction effects we start with a fraction of the atoms being already excited to a Rydberg state. Therefore, we apply two excitation pulses: the first one resonantly excites up to 20% of the atoms to the Rydberg state, whereas in the second step one laser is scanned across the resonance thereby probing the initially prepared mixture of ground state and Rydberg atoms. For comparison we also take spectra omitting the first excitation step.

The detailed experimental sequence for the double-pulse scheme is as follows: the first laser pulse is kept short (800 ns) to avoid any decoherence processes. The Rabi frequencies of this first pulse are Ω_1 = 7.2 MHz on the lower transition (780 nm) and Ω_2 = 1.4 MHz on the upper transition (480 nm). 200 ns after the first excitation pulse the probe pulse is switched on for a duration of 3 μs. For probing we keep the laser for the lower transition resonant while scanning the laser for the upper transition around the resonance. The Rabi frequencies are now chosen to be Ω_1 = 2.7 MHz on the lower and Ω_2 = 1.4 MHz on the upper transition. For these parameters on resonance the system is close to its steady state at the end of the probing time. Note that the blue laser is focused to a waist of 37 μm whereas the red laser beam has a diameter of 1 mm. Therefore, the red laser intensity can be treated as constant over the excitation volume while the Gaussian intensity distribution of the blue laser is associated with a spatial variation of Rabi frequencies. The above specified values are the peak Rabi frequencies on the upper transition. After the second pulse we ionize the Rydberg atoms by applying an electric field and we detect the resulting ions on a microchannel plate detector.

3.2. CPT in a non-interacting system

Figures 3(a) and (b) show exemplary Rydberg-CPT scans for 30S states where the amount of Rydberg atoms after the second excitation step is plotted versus the detuning of the second excitation step. At ±15 MHz the second pulse is too far away from the two-photon resonance to significantly couple the ground state to the Rydberg state. Therefore, the signal depicts the amount of Rydberg atoms excited by the first (resonant) pulse. With the frequency of the second step coming closer to resonance the light field starts to interact with the atoms, which results in Rydberg atoms being stimulated down to the fast decaying intermediate level. Hence, the Rydberg signal is reduced. On resonance the dark state is populated, which can be deduced from the subnatural resonance width. Figures 3(c) and (d) show the same scans but without the first excitation pulse. We find that, in contrast to what one would expect from

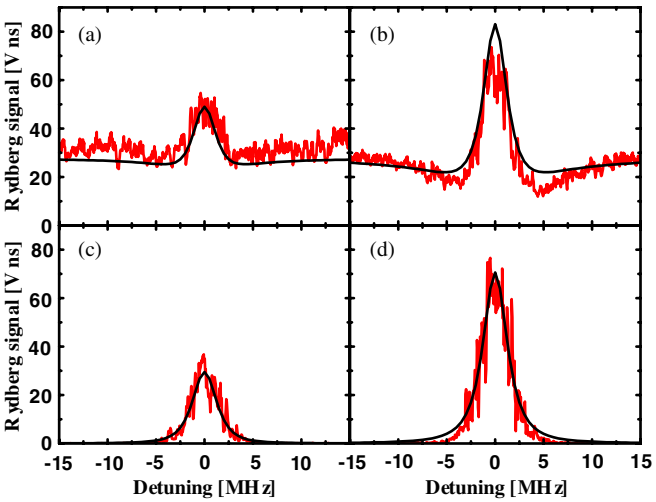

Figure 3. 30S Rydberg population as a function of the probe laser detuning Δ_2 for different peak Rabi frequencies Ω_2 of the blue probe laser, $\Omega_2 = 0.85$ MHz in (*a*) and (*c*) and $\Omega_2 = 1.7$ MHz in (*b*) and (*d*). The first excitation pulse is applied in (*a*) and (*b*), and off in (*c*) and (*d*). The red (grey) dots are measured data, the black lines are calculations based on the OBEs. The only free parameter is the absolute amplitude of the signal. This we need to adjust to make a connection between the population ρ_{33} (values between 0 and 1) and the measured signal (V*ns). However, this parameter is chosen the same for all datasets.

(1), the resonance amplitude is higher in the case of larger Rabi frequencies Ω_2. This is due to the spatial distribution of the probe Rabi frequency where Ω_2 denotes only the peak value of a Gaussian intensity distribution. Around the peak value there is a large region where due to the smaller Rabi frequencies the system has not relaxed into the dark state after 3 μs. Under these experimental circumstances it is therefore not possible to determine the Rydberg fraction using (1).

Since at typical densities in an magneto-optical trap the interatomic distance is too large for 30S atoms to interact with each other, they can be described within a single-atom picture. Including decay rates and laser linewidths as well as blackbody redistribution into the OBEs the measured spectrum can be reproduced by solving the OBE for the specific parameters of the experiment (see figure 3). Since the intermediate state is not part of the dark state (1) its natural lifetime does not contribute to the resonance width of the CPT spectrum and hence subnatural linewidths can be achieved. The laser linewidths were measured to be 1 MHz on the lower and 0.5 MHz on the upper transition. As can be seen from figure 3, the OBEs describe the non-interacting system very well independent of the chosen Rabi frequencies and independent of the starting conditions.

3.3. CPT in an interacting Rydberg system

Working with 61S states we are in a regime where interparticle interactions are expected to play a significant role as can be seen from the measured excitation blockade (see e.g. [26]). Due to the Rydberg–Rydberg interactions the measured CPT spectra with 61S Rydberg atoms show a density dependence (see figure 4) which results from the van der Waals potential

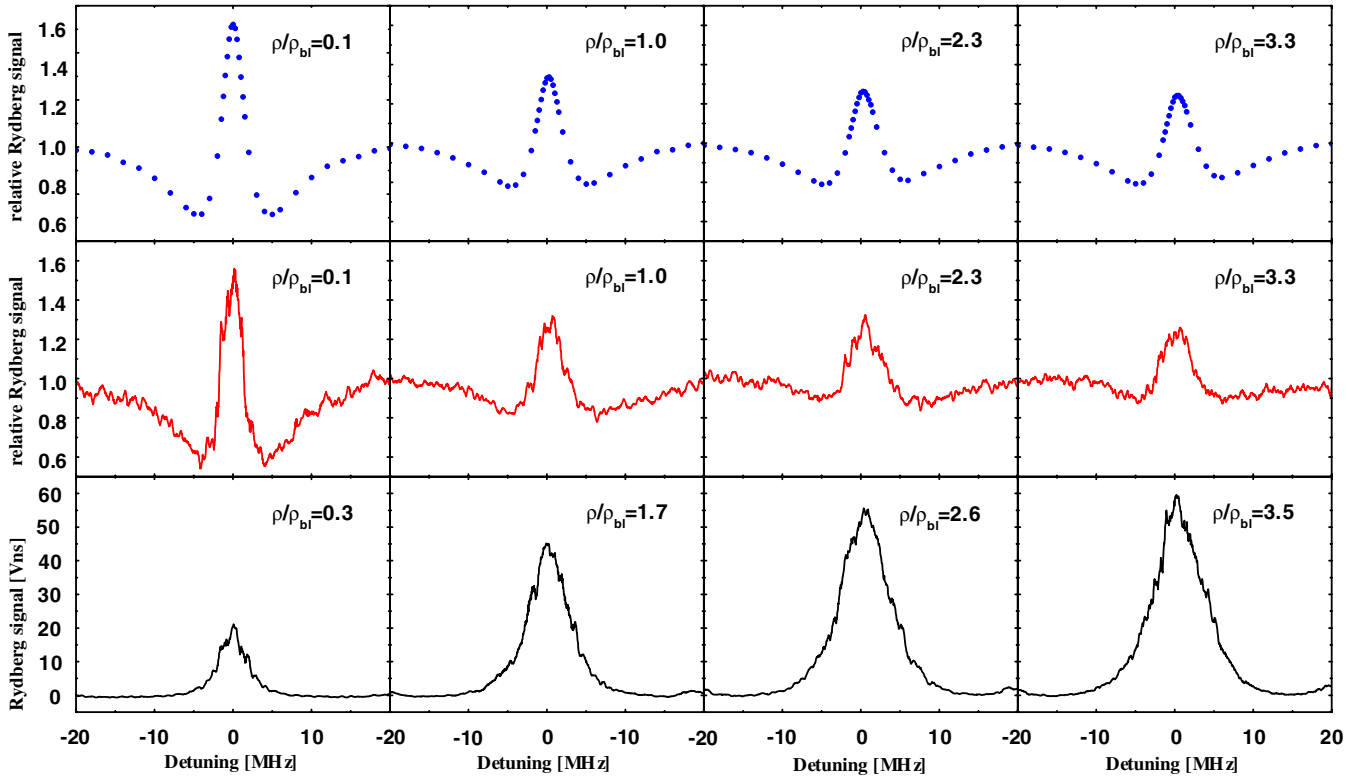

Figure 4. CPT spectra with the Rydberg state 61S obtained for different ground state atom densities, i.e. for different interaction strengths. The ground state density ρ is given relative to the density $\rho_{\rm bl} \approx 1.3 \times 10^9$ cm^{-3} at which interaction effects become apparent. $\rho_{\rm bl}$ is experimentally deduced from a blockade measurement (see e.g. [26]). The upper row shows the results obtained from the RDME approach discussed in section 2, and the second row shows experimental data. The measured as well as the calculated spectra are normalized to the asymptotic Rydberg signal at large detunings. Theory and experiment agree on a quantitative level and exhibit two main features: a reduced aspect ratio of the spectra at higher densities as well as a slight broadening of the resonance due to blockade effects. Experimentally the ground state atom density is varied by pumping a fraction of the ground state atoms into a hyperfine state which is decoupled from the excitation lasers. The last row shows CPT scans without the first excitation step for various densities (note that in contrast to the two upper rows the Rydberg signal is not plotted in relative units). The onset of CPT can be deduced from the subnatural linewidth at low densities. The side peaks at $\pm$20 MHz are due to a modulation of the blue laser which is required for laser locking.

being strongly dependent on the atomic distance. With increasing ground-state atom density we find a reduced aspect ratio of the signal as well as a slightly broadened resonance which nevertheless stays subnatural despite the strong interparticle interactions. The spectra agree on a quantitative level with the theoretical spectra obtained from the above-described reduced density matrix expansion (RDME) approach.

To realize different starting conditions for the CPT experiments the first excitation step is omitted. This leads to the spectra shown in the last row of figure 4, where we find the same central peak as in the second row, but no Rydberg signal far away from resonance. Like in the second row, the onset of CPT can be concluded from the subnatural linewidths, which are, however, broadened due to the excitation blockade at high densities.

4. EIT experiments

To explore the effect of the dipole blockade mechanism in the EIT regime, experiments are performed using the setup described in [27]. Following preparation in the $5S_{1/2}(F = 2, m_F = 2)$ ground state, a counter-propagating probe and coupling laser are used to perform EIT spectroscopy. The probe laser is scanned from $\Delta_1/2\pi = -20 \rightarrow +20$ MHz about the $5S_{1/2}(F = 2) \rightarrow 5P_{3/2}(F' = 3)$ resonance in 500 μs, whilst the coupling laser is stabilized on resonance with the $5P_{3/2}(F' = 3) \rightarrow 60S_{1/2}$ transition using an EIT locking scheme [37]. The probe and coupling lasers are tightly focussed to $1/e^2$ radii of 12 μm and 66 μm, respectively, to enhance the coupling laser Rabi frequency. Probe laser transmission is taken as a function of Ω_1, varying the probe power from 1 pW to 1 nW to measure the nonlinearity due to dipole interactions. Transmission is recorded using a single-photon counting module, taking the average of 100 measurements for each dataset.

Figure 5(a) shows data taken at a density of $\rho = 1.2 \pm 0.1 \times 10^{10}$ cm^{-3}, giving around 7000 atoms in the overlap volume of the lasers. In the weak probe regime, almost 80% transmission is observed. Fitting the spectrum to the theoretical weak-probe susceptibility enables the values of the coupling Rabi frequency and the laser linewidths to be determined, giving $\Omega_2/2\pi = 4.8$ MHz, the probe laser linewidth equal to 300 kHz and the relative two-photon laser linewidth of 110 kHz. For the $60S_{1/2}$ state the lifetime is $\sim$100 μs, giving an effective dephasing rate of 10 kHz. This

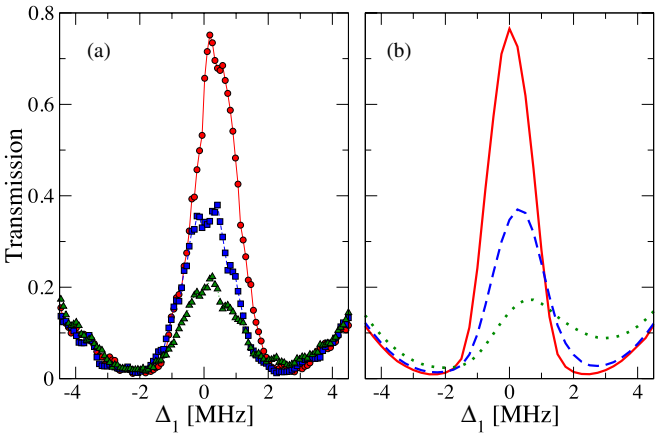

Figure 5. Probe-beam transmission spectrum for different probe powers corresponding to $\Omega_1 = 0.3$ MHz (circles, solid line), 1.0 MHz (squares, dashed line) and 2.0 MHz (triangles, dotted line) at a peak density of 1.2×10^{10} cm^{-3} and $\Omega_2 = 4.8$ MHz. The two panels compare experimental data (a) to the theoretical MCRE results (b), showing good agreement for the resonant transmission.

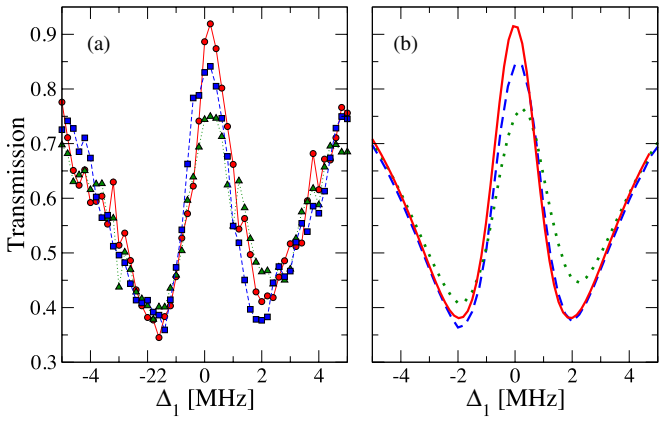

Figure 6. Probe-beam transmission spectrum for different probe powers corresponding to $\Omega_1 = 0.08$ MHz (circles, solid line), 1.1 MHz (squares, dashed line) and 2.0 MHz (triangles, dotted line) at a peak density of 3.5×10^9 cm^{-3} and $\Omega_2 = 3.8$ MHz. The two panels compare experimental data (a) to the theoretical MCRE results (b), showing good agreement for the resonant transmission.

is much smaller than the two-photon laser linewidth which is the dominant dephasing mechanism. The combination of the dephasing and power broadening gives an FWHM of the EIT resonance of 2 MHz.

As the probe power is increased the interactions modify the EIT dark state within each blockade sphere, mixing in the intermediate excited state which resonantly couples to the probe beam. This can be seen from the suppression of the resonant transmission to around 20% at $\Omega_1/2\pi = 2.0$ MHz. Since there is neither a shift nor a broadening of the data, this rules out ionization or dephasing as the suppression mechanism [27].

Figure 5(b) shows our theoretical transmission spectrum calculated using the Monte Carlo rate equation (MCRE) approach described above. In these calculations we use the value above for the Rabi frequency Ω_2 and determine the relative laser linewidths from the measured transmission spectrum in the non-interacting, weak probe regime given above. The results are then averaged over the experimentally determined density distribution of the cloud and Gaussian intensity profiles of the lasers. The theory shows very good agreement with experiment for the resonant transmission with no fitting parameters. The lineshape of the high-intensity spectrum, however, displays an asymmetry not observed in the experiment. The asymmetry in the theory arises from resonances with the shifted Rydberg pair states, leading to a reduction in the ground- and intermediate-state population. We note that the theory assumes classical pulses and neglects photon–photon correlations, such that the observed deviations could be an indication of interaction-modified photon counting statistics not covered by the theory. In addition, the absence of the asymmetry in the experiments could be caused by motion of the atoms due to the strong van der Waals interactions. The latter are repulsive for the $nS_{1/2}$ states and, thus, cause atoms to be accelerated away from each other. For a pair of atoms with 6 μm separation, the interaction shift is 3 MHz. After 38 μs, which is the time required to scan the probe laser by 3 MHz, this separation increases to $R \simeq 10$ μm, which corresponds to $V(R) = 0.5$ MHz. Hence, initially resonant atoms move out of resonance during the probe scan, leading to a larger absorption than obtained theoretically under the frozen gas assumption.

This paper is supported by the good agreement between theory and experiment at lower densities (see figure 6), for which asymmetries are found in both the experimental and theoretical data. Since the mean interparticle distance is larger at lower densities, motional effects due to pair repulsion are expected to become less important with decreasing density.

5. Universal scaling

The two experiments discussed in sections 3 and 4 cover the regimes of large and small Rydberg admixture. In section 3 ($\Omega_1 > \Omega_2$), we have measured the narrow Rydberg excitation line arising from CPT, by probing the Rydberg population ρ_{33}, which directly yields the fraction $f_{\rm bl}$ of interaction-blocked Rydberg excitations. In section 4, measurement of the transmission in the weak excitation regime ($\Omega_1 < \Omega_2$) gave direct information about the probe-beam optical susceptibility χ_{12}, demonstrating EIT and its nonlinear modification due to the strong interactions. As shown recently using the presented MCRE approach [36], these quantities, $f_{\rm bl}$ and χ_{12}, are connected by a simple universal relation

$$\tilde{\chi}_{12} = \frac{f_{\rm bl} + \tilde{\chi}_{12}^{(0)}}{1 + f_{\rm bl}} \tag{5}$$

upon scaling the three-level susceptibility by the corresponding two-level value $\chi_{12}^{(2{\rm lv})}$, i.e. $\tilde{\chi}_{12} = \chi_{12}/\chi_{12}^{(2{\rm lv})}$. $\tilde{\chi}_{12}^{(0)}$ denotes the scaled susceptibility for non-interacting atoms arising from the finite linewidth of the excitation lasers. As shown in figure 7, this simple scaling allows the two different experiments to be related, showing that they, in fact, cover overlapping regimes in terms of the realized blockade fractions and scaled susceptibilities. Future merging of the

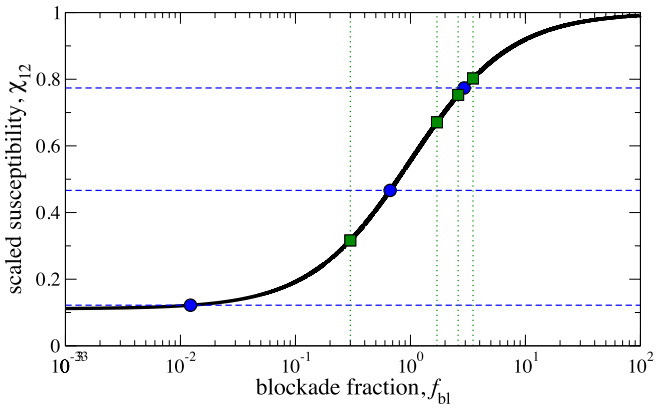

Figure 7. Universal relation between the scaled susceptibility $\tilde{\chi}_{12} = \chi_{12}/\chi_{12}^{(2lv)}$ and the fraction f_{bl} of interaction-blocked Rydberg excitations. The horizontal and vertical lines mark our measurements of the blockade fraction (squares and dotted lines), figure 4(c), and of the probe-beam transmission (circles and dashed lines), figure 5(a).

two presented experimental approaches to simultaneously measure the Rydberg population and the probe transmission should allow verification of this universal relation between the interaction blockade and the nonlinear optical response of a Rydberg-EIT medium.

6. Conclusion

In this work, we have presented a joint experimental and theoretical study of three-level interference effects in a strongly interacting Rydberg gas, covering the regimes of weak Rydberg state admixture and strong Rydberg excitation. We show that the experimental observations are accurately described using a many-body approach based on either a reduced many-particle density matrix or a Monte Carlo sampling of the excitation rate. We point out a universal scaling of the optical response with the Rydberg blockade fraction and suggest how the combination of the two experimental techniques presented could enable experimental verification of this property.

Acknowledgments

This work was supported by the Heidelberg Center for Quantum Dynamics, the Deutsche Forschungsgemeinschaft (grant no WE2661/10-1), the UK Engineering and Physical Sciences Research Council, and Durham University.

References

[1] Harris S E, Field J E and Imamoglu A 1990 *Phys. Rev. Lett.* **64** 1107
[2] Bergmann *et al* 1998 *Rev. Mod. Phys.* **70** 1003
[3] Boller K-J, Imamoglu A and Harris S E 1991 *Phys. Rev. Lett.* **66** 2593
[4] Hau L V *et al* 1999 *Nature* **397** 594
[5] Fleischhauer M, Imamoğlu A and Marangos J P 2005 *Rev. Mod. Phys.* **77** 633
[6] Santori C *et al* 2006 *Phys. Rev. Lett.* **97** 247401
[7] Thévenaz L 2008 *Nat Photon.* **2** 474
[8] Xu X *et al* 2008 *Nat Phys.* **4** 692
[9] Weis S *et al* 2010 *Science* **330** 1520
[10] Gray H R *et al* 1978 *Opt. Lett.* **3** 218
[11] Harris S E 1997 *Phys. Today* **50** 36
[12] Lukin M D 2003 *Rev. Mod. Phys.* **75** 457
[13] Gorshkov A V *et al* 2007 *Phys. Rev. Lett.* **98** 123601
Gorshkov A V *et al* 2007 *Phys. Rev.* A **76** 033804
Gorshkov A V *et al* 2007 *Phys. Rev.* A **76** 033805
Gorshkov A V *et al* 2007 *Phys. Rev.* A **76** 033806
[14] Lukin M D and Imamoglu A 2000 *Phys. Rev. Lett.* **84** 1419
[15] Santra R *et al* 2005 *Phys. Rev. Lett.* **94** 173002
[16] Mohapatra A K, Jackson T R and Adams C S 2007 *Phys. Rev. Lett.* **98** 113003
[17] Pohl T, Demler E and Lukin M D 2010 *Phys. Rev. Lett.* **104** 043002
[18] Olmos B and Lesanovsky I 2010 *Phys. Rev.* A **82** 063404
[19] Møller D, Madsen L B and Mølmer K 2008 *Phys. Rev. Lett.* **100** 170504
[20] Müller M, Lesanovski I, Weimer H, Büchler H P and Zoller P 2009 *Phys. Rev. Lett.* **102** 170502
[21] Friedler I *et al* 2005 *Phys. Rev.* A **72** 043803
[22] Weimer H, Müller M, Lesanovski I, Zoller P and Büchler H P 2010 *Nat Phys.* **6** 382
[23] Weatherill K J *et al* 2008 *J. Phys. B: At. Mol. Opt. Phys.* **41** 201002
[24] Mohapatra A K, Bason M G, Butscher B, Weatherill K J and Adams C S 2008 *Nat Phys.* **4** 890
[25] Raitzsch U *et al* 2009 *New J. Phys.* **11** 055014
[26] Schempp H *et al* 2010 *Phys. Rev. Lett.* **104** 173602
[27] Pritchard J D *et al* 2010 *Phys. Rev. Lett.* **105** 193603
[28] Lukin M D *et al* 2001 *Phys. Rev. Lett.* **87** 037901
[29] Amthor T *et al* 2007 *Phys. Rev. Lett.* **98** 023004
Amthor T *et al* 2007 *Phys. Rev.* A **76** 054702
[30] Younge K C *et al* 2009 *Phys. Rev.* A **79** 043420
[31] Pohl T and Berman P R 2009 *Phys. Rev. Lett.* **102** 013004
[32] Bogoliubov N N and Bogoliubov N N Jr 1992 *Introduction to Quantum Statistical Mechanics* (Singapore: Gordon and Breach)
[33] Ates C *et al* 2006 *J. Phys. B: At. Mol. Opt. Phys.* **39** L233
Ates C *et al* 2007 *Phys. Rev. Lett.* **98** 023002
[34] Ates C *et al* 2007 *Phys. Rev.* A **76** 013413
[35] Lesanovsky I, Olmos B and Garrahan J P 2010 *Phys. Rev. Lett.* **105** 100603
[36] Ates C, Sevinçli S and Pohl T 2011 *Phys. Rev.* A **83** 041802
[37] Abel R P *et al* 2009 *Appl. Phys. Lett.* **94** 071107